Crisp-BP: Continuous Wrist PPG-based Blood Pressure Measurement

Yetong Cao
School of Computer Science
Beijing Institute of Technology
yetongcao@bit.edu.cn

Huijie Chen
School of Computer Science
Beijing University of Technology
chenhuijie@bjut.edu.cn

Fan Li*
School of Computer Science
Beijing Institute of Technology
fli@bit.edu.cn

Yu Wang
Department of Computer and Information Sciences
Temple University
wangyu@temple.edu

ABSTRACT

Arterial blood pressure (ABP) monitoring using wearables has emerged as a promising approach to empower users with self-monitoring for effective diagnosis and control of hypertension. However, existing schemes mainly monitor ABP at discrete time intervals, involve some form of user effort, have insufficient accuracy, and require collecting sufficient training data for model development. To tackle these problems, we propose *Crisp-BP*, a novel ABP monitoring system leveraging the PPG sensor available in commercial wrist-worn devices (e.g., smartwatches or fitness trackers). It enables continuous, accurate, user-independent ABP monitoring and requires no behavior changes during collecting PPG data. The basic idea is to illuminate a skin/tissue, measure the light absorption, and characterize ABP-related blood volume change in the artery. To obtain accurate measurements and relieve the pain of training data collection, we use an arterial pulse extraction method that removes interference caused by capillary pulses. Moreover, we design a contact pressure estimation method to combat the deficiency of PPG waveform being sensitive to the contact pressure between the sensor and the skin. In addition, we leverage the great power of *Bidirectional Long Short Term Memory* and design a hybrid neural network model to enable user-independent ABP monitoring, so that users do not have to provide training data for model development. Furthermore, we propose a transfer learning method that first extracts general knowledge from online PPG data, then use it to improve the learning of a new model on our target problem. Extensive experiments with 35 participants demonstrate that *Crisp-BP* obtains the average estimation error of 0.86 mmHg and 1.67 mmHg and the standard deviation error of 6.55 mmHg and 7.31 mmHg for diastolic pressure and systolic pressure, respectively. These errors are within the acceptable range regulated by the FDA's AAMI protocol, which allows average errors of up to 5 mmHg and a standard deviation of up to 8 mmHg. Our results demonstrate that *Crisp-BP* is promising for improving the diagnosis and control of hypertension as it provides continuousness, comfort, convenience, and accuracy.

CCS CONCEPTS

• **Human-centered computing → Ubiquitous and mobile computing systems and tools**.

KEYWORDS

blood pressure, contact pressure, neural networks, BLSTM, PPG sensing

ACM Reference Format:
Yetong Cao, Huijie Chen, Fan Li, and Yu Wang. 2022. Crisp-BP: Continuous Wrist PPG-based Blood Pressure Measurement. In *The 27th Annual International Conference on Mobile Computing and Networking (ACM MobiCom '21), January 31-February 4, 2022, New Orleans, LA, USA.* ACM, New York, NY, USA, 14 pages. https://doi.org/10.1145/3447993.3483241

1 INTRODUCTION

Hypertension has become a global health issue, and it is a major cause of premature death and disability [36]. Specifically, global estimates suggest that upwards of one in four men and one in five women have hypertension, and the prevalence is expected to increase owing to the aging of the population. What was worse, hypertension rarely has symptoms (like a silent killer), which makes it difficult for early prevention and diagnosis unless accurate blood pressure is obtained. Recently, many efforts have been made for accurate ABP monitoring (e.g., auscultation [54], oscillations [44], volume clamp [42], tonometry [43], and ultrasound [13]). However, these technologies usually need to compress the vessel during ABP measuring procedure, which makes them uncomfortable and brings tissue hypoxia risks [23]. Besides, these technologies are difficult to be widely adopted in daily life due to the requirement of special equipment (high price, large size, and complex operation).

The popularity of wearable devices makes it possible to enable portable ABP measurements in daily life. For example, HeartGuide [8] and eBP [14] enable oscillometric measurements of ABP in wristwatch and in-ear wearable, respectively. These schemes will block the user's blood vessels for a long time, which makes them uncomfortable.

*Fan Li is the corresponding author.

ACM MobiCom '21, January 31-February 4, 2022, New Orleans, LA, USA

ACM ISBN 978-1-4503-8342-4/22/01…$15.00
https://doi.org/10.1145/3447993.3483241

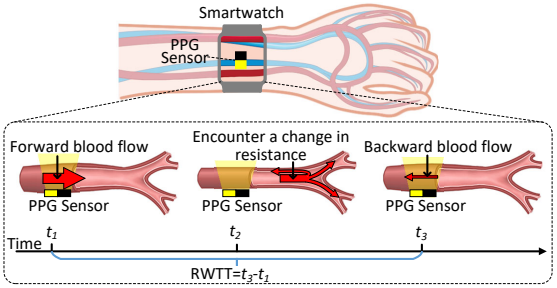

Figure 1: An illustration of RWTT estimation with a single PPG sensor.

Afterward, the electrocardiography (ECG) and photoplethysmography (PPG) sensors are utilized for wristband ABP measuring (e.g., Apple Watch [6] and VivoWatch [2]), which target to reduce the discomfort. The corresponding technologies mainly rely on the close correlation between the ABP and the interval time between ECG and PPG (defined as pulse arrival time (PAT) [19, 28] and pulse transit time (PTT) [38, 40] in the medical field). However, users are still burdened due to the necessary user effort (i.e., users need to cover the ECG pad with their fingers) throughout data collection. Thus, wearable ABP monitors without requiring user effort are proposed, such as glasses [25] and compression shorts [16]. However, they are restricted to limited scenarios (i.e., works in daytime and night, respectively) and their performance is always influenced by many factors (e.g., season effects, time of day, and temperature). Besides, machine learning algorithms are also adopted to improve the accuracy by extracting features from ECG and PPG [21, 47, 58]. However, collecting sufficient training data is inconvenient and usually takes a lot of effort.

These limitations motivate us to design and implement ***Crisp-BP***, a ***C**ontinuous **W**rist **P**PG-based **B**lood **P**ressure monitoring system*. The design is inspired by our observation that ABP values can be estimated from the reflected wave transit time (RWTT) with only a single PPG sensor available in commercial wrist-worn devices (e.g., smartwatches or fitness trackers). Specifically, blood encounters a change in resistance when traveling at the bifurcations in the arterial tree, causing part of the blood flow to travel backward (as shown in Fig. 1). Then, RWTT represents the transit time between the forward blood flow and the backward blood flow at the same position and can be used for ABP estimation [51, 57]. Besides, the forward blood flow and backward blood flow successively induce volume changes in the artery. The volume changes cause light absorption changes that can be captured with a PPG sensor. Therefore, *Crisp-BP* estimates the RWTT through profiling the changing pattern of blood volume with the captured light reflection intensity. Then, the continuous ABP is obtained.

Despite this simple idea, three major challenges underlie the design:

- To obtain accurate RWTT, we characterize the volume changes in the artery based on PPG data. However, the collected PPG data are inevitably interfered with volume changes in the superficial capillary bed, which arrives at a different time from the volume changes in the artery. Such a phenomenon causes errors in RWTT estimates. To address this, we associate the wavelength-dependent PPG with the skin vasculatures and remove capillary interference based on the modified Beer-Lambert law.
- PPG waveform is highly sensitive to the contact pressure between the sensor and human skin, making it extremely hard to extract reliable PPG data for ABP monitoring. To address contact pressure artifact, we design a Least-Squares Support Vector Machine (LSSVM)-based method to estimate contact pressure, then assist users in adjusting the wearable tight or loose and maintain a proper contact pressure during data collection.
- Existing approaches require collecting sufficient data from each user for developing user-specific models. However, it is inconvenient and usually takes a lot of effort. In contrast, we propose a user-independent ABP monitoring model with a hybrid network based on Bidirectional Long Short Term Memory (BLSTM). Furthermore, we design a transfer learning method to improve the ABP measurement accuracy.

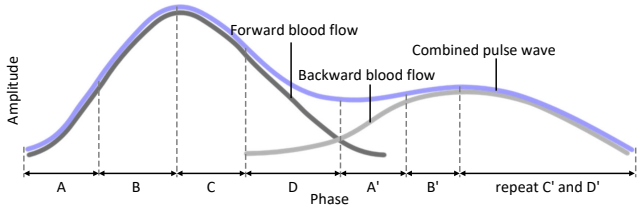

(a) Example of forward blood flow, backward blood flow, and pulse wave

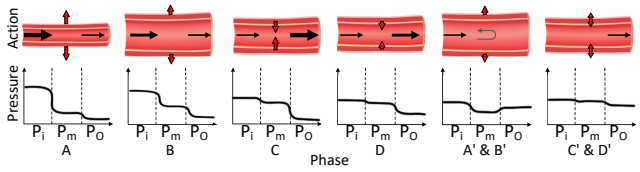

(b) Vessel wall movement and pressure gradients

Figure 2: An example of pulse wave, and vessel wall movements [46].

Our major contributions are summarized as follows:

- We demonstrate that a single commodity PPG sensor available in wrist-worn devices can be used to measure RWTT and produce measurements of ABP. We develop *Crisp-BP*, which is the first to present an accurate and user-independent ABP monitoring system. It is low-cost, comfortable, convenient, and supports long-term monitoring, which makes it suitable to be adopted widely.
- We design a set of techniques, including an arterial pulse extraction method and a contact pressure estimation algorithm that overcomes the capillary interference and contact-pressure-sensitive deficiency in PPG signals. In addition, we design a BLSTM-based hybrid network for user-independent ABP monitoring. Furthermore, we propose a transfer learning method that extracts general knowledge from online PPG data, then use it to improve the learning of the model of our problem.
- We implement *Crisp-BP* and evaluate it with 35 participants under various parameters and scenarios. The results show

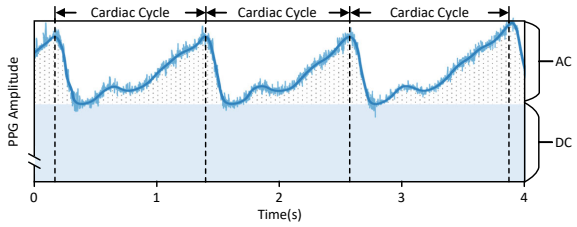

Figure 3: An illustration of a reflective PPG waveform, showing mirrored rule due to reflective measurement.

that *Crisp-BP* obtains the estimation error of 0.86 ± 6.55 mmHg and 1.67 ± 7.31 mmHg for diastolic blood pressure (DBP) and systolic blood pressure (SBP), respectively.

The rest of this paper is organized as follows: Section 2 introduces the background knowledge. Section 3 presents the system overview, followed by the detailed system designs in Section 4 and Section 5. Evaluation and discussion are presented in Section 7 and Section 8, respectively. Section 9 reviews the related work. Finally, we draw our conclusion in Section 10.

2 BACKGROUND

2.1 Basic of Pulse Wave

The pulse wave is affected by the forward blood flow and the backward blood flow. Considering the blood vessel as an elastic tube, the inner volumes and vessel diameter is varied by the pressure difference of the input (P_i), measurement spot (P_m), and output (P_o). As shown in Fig. 2, a pulse starts with the systole (phase A). Then, the blood volume rapidly increases because the pressure difference is large between P_i and P_m (phase B). Such an increase is rapidly reduced subsequently by the diminishing of the pressure gradients. In the early-diastole, the pressure gradient between P_m and P_o increases, and rapid outflow occurs (phase C). While in the late-diastole, the outflow is diminished with the decreasing of the pressure gradient between P_m and P_o (phase D). After the backward blood flow occurs, P_o increases, resulting in decreased output pressure gradients. This change suppresses outflow, causing the blood volume to increase at the measuring position (phase A' and phase B'). Successively arrived multiple backward blood flow cause fluctuation of P_o and blood volume (phase C' and phase D').

2.2 Basic of Photoplethysmography (PPG)

PPG is a simple and inexpensive optical technique that detects the blood volume by illuminating a skin/tissue and measuring the light absorption. In recent years, wrist-worn devices equipped with PPG sensors have grown dramatically. These PPG sensors are mainly designed to collect pulse waves and monitor heart rates in routine health care applications. With the fast pace of technological advancement, more and more devices use the combination of infrared and green light as light sources, such as Apple Watch [6], Huawei Watch [4], Honor Band [3], and Xiaomi Band [5].

Fig. 3 shows a typical waveform of a reflective PPG signal obtained at the wrist, showing mirrored rule due to reflective measurement principle. The PPG waveform shows the vessel extension caused by the change of blood volume, which has a similar appearance with blood pressure wave [22]. The PPG signal consists of an

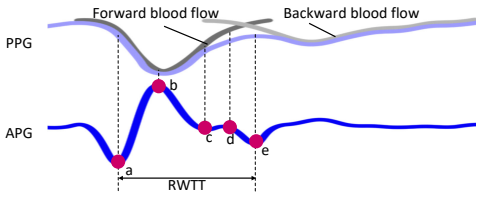

Figure 4: An illustration of reflective PPG and APG.

alternating component (AC) and a direct current (DC) component. The AC component is attributed to the changes in the blood volume with each heartbeat [10]. Whereas the DC component is based on reflected and scattered light from the venous and tissue layers, which are the components without a pulsatile signal [11].

2.3 Intuition of Measuring RWTT using Acceleration Photoplethysmography

The second derivative of the PPG signal, referred to as acceleration photoplethysmography (APG), is a popular technique for pulse wave analysis. Previous researches demonstrate that the APG amplifies higher frequencies and allows more precise temporal analysis than the original PPG.

When the forward blood flow and backward blood flow successively travel through the artery, blood volume undergoes delicate changes. The blood volume V can be expressed as the product of a sectional area S in the vessel and the length L of a blood-contained portion: $V = S \cdot L$. The quadratic differentiation of V at time t can be written as [41]:

$$\frac{d^2V}{dt^2} = 2 \cdot \frac{dS}{dt} \cdot \frac{dL}{dt} + L \cdot \frac{d^2S}{dt^2} + S \cdot \frac{d^2L}{dt^2}. \quad (1)$$

The terms on the right side represent (1) the product of blood flow speed and the expansion speed of the vessel, (2) the product of the expansion acceleration of the vessel and the length of the said portion, and (3) the product of the blood flow acceleration and the sectional area of the blood contained portion. Because the blood pressure influences the blood flow speed and blood flow acceleration, the quadratic differentiation of V implies the change in blood speed produced in response to a delicate change in artery pressure. APG is considered the quadratic differentiation of V as it shows the change in acceleration of blood volume in the artery. Therefore, we derive the RWTT from APG. Specifically, as shown in Fig. 4, APG waveform characteristically exhibits five fiducial points. RWTT is defined as the time delay between the forward blood flow and the backward blood flow at the same position. In this work, RWTT is measured as the interval between the systolic slope (a) and the arrival of the backward blood flow at the augmentation point (e).

3 SYSTEM OVERVIEW

Crisp-BP captures the RWTT-related blood volume change in the artery using a commodity two-wavelength PPG sensor. As illustrated in Fig. 5, *Crisp-BP* is mainly comprised of four models: *Two-Wavelength Light Sensing*, *Device State Identification*, *Arterial Pulse Profiling*, and *Continuous ABP Monitoring*.

In *Two-Wavelength Light Sensing*, the PPG sensor switches green and infrared light on for 0.4 ms in turn with a 0.1 ms interval

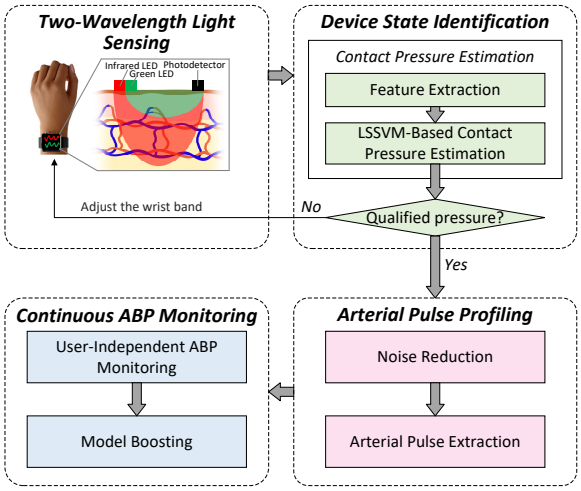

Figure 5: *Crisp-BP* framework.

in which all LEDs are turned off. Meanwhile, the light reflection is captured by the PPG sensor and will be input into the next component.

Then, *Crisp-BP* performs *Device State Identification* to determine whether the contact pressure between the PPG sensor and skin is qualified. For that, *Crisp-BP* selects two features to represent the changes in vascular elasticity and vascular resistance under different contact pressures. Then, the contact pressure is estimated using the Least-Squares Support Vector Machine (LSSVM). After that, *Crisp-BP* guides the user to tight or loose the wristband so that the contact pressure is close to the optimal contact pressure.

Then, the obtained PPG data are served to *Arterial Pulse Profiling*. In *Arterial Pulse Profiling*, *Crisp-BP* first removes noises in the PPG data in *Noise Reduction*, then extracts arterial pulse based on the modified Beer-Lambert law in *Arterial Pulse Extraction*.

After that, *Crisp-BP* conducts *Continuous ABP Monitoring*. We first detect fiducial points by locating extremes of APG signal to measure RWTT. To enable accurate and user-independent ABP monitoring, *Crisp-BP* extracts RWTT and supplement features (personal information and vascular characteristics) and constructs a hybrid neural network based on Bidirectional Long Short Term Memory (BLSTM). Furthermore, to boost *Crisp-BP* and alleviate the pain of collecting sufficient training data from all ages and genders, we propose a transfer learning method. The transfer learning method can extract general knowledge from online PPG data then transfer it to a new model in *Crisp-BP*'s domain. We next introduce the details of *Device State Identification*, *Arterial Pulse Profiling*, and *Continuous ABP Monitoring*.

4 DEVICE STATE IDENTIFICATION

4.1 Impact of Contact Pressure

The PPG waveform is highly sensitive to the contact pressure between the sensor and human skin [18]. On the one hand, when the PPG sensor contacts the skin loosely, the inappropriate contact pressure introduces noise data related to the motion artifacts. On the other hand, when the PPG sensor contacts the skin too tightly, the changes in the blood volume are difficult to be detected due to

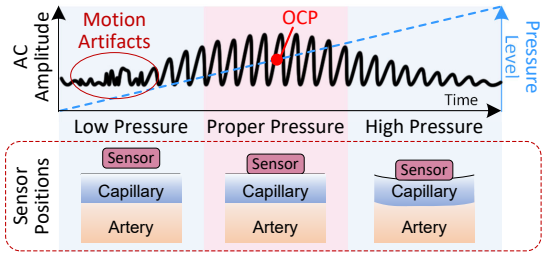

Figure 6: An illustration of the relationship between contact pressure and PPG pulsation waveform.

vessel occlusion. Therefore, keeping appropriate contact pressure is vital in *Crisp-BP* for accurate ABP measuring.

Fig. 6 illustrates the relationship between diverse contact pressures and the corresponding PPG pulsation waveforms (AC component) collected at the wrist. We can observe that pulsation waveform amplitude increases and then decreases with the increasing contact pressure. Similar conclusions can be drawn in studies of contact pressure applied to the finger [18, 26].

4.2 Contact Pressure Estimation

4.2.1 Feature Extraction. When the PPG sensor applies pressure to the skin, deformations are introduced to the blood vessels and skin tissues, which affects the recovery of blood vessels and the blood flow resistance. These changes can be described by features related to vascular elasticity and vascular resistance, such as *pulse widths*, *the ratio of time interval between systolic phase and diastolic phase*, *pulse propagation time*, *the ratio of diastolic area to systolic area*, *the ratio of the amplitude of systolic peak to that of diastolic peak*,and *total areal of a pulse*, etc.

To avoids the unreliable results caused by extracting plenty of features, we detect the multicollinearity between these features by comparing the Variance Inflation Factor (VIF). Thus, two significant features with the lowest VIF are selected (i.e., F_1*: the ratio of the time interval between systolic phase and diastolic phase*, and F_2*: the ratio of the amplitude of systolic peak to that of diastolic peak*). Specifically, F_1 is measured as the ratio of the interval from the start point and b to the interval from b and the end point in APG data. F_2 is measured as the ratio of the amplitude of PPG signal at the time when a and b in APG signal occur.

4.2.2 LSSVM-Based Contact Pressure Estimation. Contact pressure estimation is a major challenge since the influence of the extracted features on contact pressure is still rather vague. Due to the fact that least-squares support vector machine (LSSVM) is capable of dealing with an ill-posed problem caused by a few training data [50, 52], LSSVM is adopted to train a fitting function that describes the relationship between contact pressure and extracted features. The training procedure is offline. Specifically, LSSVM is a statistical learning technique that adopts a least-squares linear system as a loss function. By using the quadratic cost function, the optimization problem is reduced to solve a set of linear equations. Then, when a user accesses to *Crisp-BP*, we extract features as described in Section 4.2.1, and estimate beat-to-beat contact pressure using the pre-trained LSSVM.

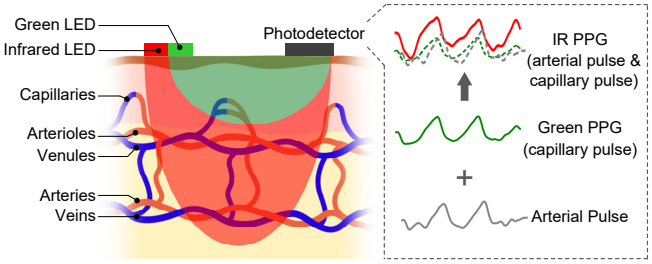

Figure 7: An illustration of PPG waveform and skin vasculatures.

4.2.3 Contact Pressure Qualification. Through experiments (presented in Section 7.4.1), we find that the system achieves the best performance under the optimal contact pressure (OCP), which manifests in the form of the highest amplitude of the AC component (shown in Fig. 6). Therefore, users are encouraged to collect PPG data at or near the OCP, which are considered qualified contact pressures. However, the OCP varies greatly from the individual involved. Besides, the changes in the human body (e.g., losing weight, sweating) and different measuring positions can lead to different OCPs. It is difficult for users without professional knowledge to determine whether the wristband should be adjusted tight or loose according to contact pressure values. Thus, a calibration procedure is introduced to help determine the OCP. Every time the user puts on the smartwatch, we ask him/her to slowly press the wrist-worn device, increase contact pressure until the PPG AC component completely disappears, then slowly release the device, reduce contact pressure until the PPG sensor loose contact with the skin. We use the trained LSSVM to estimate the pressure at the highest amplitude of the AC component, i.e., OCP. When the current contact pressure is greater than the OCP, *Crisp-BP* guides the user to tight the wristband and otherwise would guide the user to loose the wristband. Overall, *Crisp-BP* achieves effectiveness in contact pressure estimation, which is demonstrated through experiments in Section 7.4.1.

5 ARTERIAL PULSE PROFILING

5.1 Noise Reduction

Human heart rate generally ranges from 60 to 100 beats per minute. We first apply a fourth-order Butterworth filter with cutoff frequencies of [0.5-8] Hz to remove interference caused by baseband drift and power-line. Then, we roughly segment the beat-to-beat sequence using the filter of intervals between successive normal complexes. After that, we use the percentage change method [33] to remove motion artifacts and other outlier pulses, which is defined as having an interbeat interval deviating more than 30% from the mean of the four previous accepted intervals.

5.2 Arterial Pulse Extraction

Intuition: *Crisp-BP* performs ABP measuring with an accurate RWTT, which is estimated through profiling the changing pattern of blood volume with a single PPG sensor. However, the collected PPG data are inevitably interfered with volume changes in the superficial capillary bed, which reduces the accuracy of RWTT estimation. To address this, we associate the wavelength-dependent PPG with the skin vasculatures and remove capillary interference based on the modified Beer-Lambert law [12]. Specifically, a typical PPG sensor on wearables employs green and infrared light emitters and a photodetector. Green light can reach the superficial capillaries. Infrared light can penetrate through the skin and reach the arteries in the subcutaneous tissue. Therefore, PPG data collected in green light (denoted as green PPG) carry capillary pulses while PPG collected in infrared light (denoted as IR PPG) carry a complex result of concurrent pulses of capillary and arterial, as shown in Fig. 7. Arterioles are small branches of the artery leading into capillaries, and arteriole pulses are negligible in this work. To associate the wavelength-dependent light penetration depth in the skin with skin vasculatures, we adopt the modified Beer-Lambert law. The modified Beer-Lambert law is reported useful in relating changes in the optical density to changes in tissue absorption.

Optical Density Modeling: During cardiac cycles, the blood volume changes introduce changes in the reflected optical density (ΔOD) captured by the PPG sensor. The general expression for homogeneous tissue is defined as the negative logarithm of the ratio between the detected light intensity $I(t)$ and the incident light intensity I^0 [12]:

$$\begin{aligned}\Delta OD(t) &= -\log\left(\frac{I(t)}{I^0}\right)\\ &\approx \langle L\rangle\,\Delta\mu_a(t) + \left(\frac{\mu_a^0}{\mu_s'^0}\right)\langle L\rangle\,\Delta\mu_s'(t)\\ &\approx \langle L\rangle\,\Delta\mu_a(t),\end{aligned} \tag{2}$$

where $\langle L\rangle \equiv \partial OD^0/\partial\mu_a$ is the differential path length, OD^0 is the baseline optical density. μ_a^0 and $\mu_s'^0$ are baseline absorption coefficient and scattering coefficient, respectively. $\Delta\mu_a(t)$ is the differential changes in absorption, which is modeled by $\Delta\mu_a(t) = \varepsilon\cdot\Delta C(t)$, where $\Delta C(t)$ is the change of the volume faction of blood , ε is the absorption coefficient of the turbid tissue. The tissue scattering changes $\Delta\mu_s'(t)$ that typically accompany hemodynamic concentration variations are often negligible.

We simplify the cutaneous vasculature and tissues as two layers of homogeneous medium. The incident green light at wavelength λ_g can reach the first layer (capillary), and the incident infrared light at wavelength λ_{IR} can travel through the first layer and the second layer (arteriole and artery). The change in optical density can be expressed as:

$$\begin{cases}\Delta OD^{\lambda_g}(t) = \left\langle L_1^{\lambda_g}\right\rangle\cdot\varepsilon_1^{\lambda_g}\cdot\Delta C_1(t)\\ \Delta OD^{\lambda_{IR}}(t) = \left\langle L_1^{\lambda_{IR}}\right\rangle\cdot\varepsilon_1^{\lambda_{IR}}\cdot\Delta C_1(t)\\ \qquad\qquad + \left\langle L_2^{\lambda_{IR}}\right\rangle\cdot\varepsilon_2^{\lambda_{IR}}\cdot\Delta C_2(t),\end{cases} \tag{3}$$

where subscripts 1 and 2 represent the coefficient at the first and second layer, respectively.

Arterial Pulse Modeling: arterial pulse $\Delta C_2(t)$ can be derived using:

$$\Delta C_2(t) = \frac{\Delta OD^{\lambda_{IR}}(t) - \frac{\left\langle L_1^{\lambda_{IR}}\right\rangle\cdot\varepsilon_1^{\lambda_{IR}}}{\left\langle L_1^{\lambda_g}\right\rangle\cdot\varepsilon_1^{\lambda_g}}\Delta OD^{\lambda_g}(t)}{\left\langle L_2^{\lambda_{IR}}\right\rangle\cdot\varepsilon_2^{\lambda_{IR}}}. \tag{4}$$

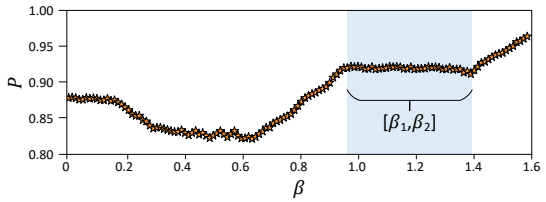

Figure 8: An example of beat-to-beat duration correlation P change along different β.

We rewrite Equ. 4 to the following expression:

$$\Delta C_2(t) = \frac{\Delta OD^{\lambda_{IR}}(t) - \beta \cdot \Delta OD^{\lambda_g}(t)}{\alpha}. \tag{5}$$

We consider α as the scaling coefficient. Since we are interested in the time reference of arterial pulse to measure RWTT, we focus on identifying the value of β. By defining:

$$\begin{aligned} \Delta d(\beta, t) &= \Delta OD^{\lambda_{IR}}(t) - \beta \cdot \Delta OD^{\lambda_g}(t) \\ &= [\left\langle L_1^{\lambda_{IR}} \right\rangle \cdot \varepsilon_1^{\lambda_{IR}} - \beta \left\langle L_1^{\lambda_g} \right\rangle \cdot \varepsilon_1^{\lambda_g}] \cdot \Delta C_1(t) \\ &+ \left\langle L_2^{\lambda_{IR}} \right\rangle \cdot \varepsilon_2^{\lambda_{IR}} \cdot \Delta C_2(t), \end{aligned} \tag{6}$$

we turn the problem of estimating β into finding the correct value of β where $\Delta d(\beta, t)$ is dominated by $\Delta C_2(t)$.

Problem Solving: in practice, since the vessels are distributed in a layer with certain thickness, there is a subrange of β within $[\beta_1, \beta_2]$ where $\Delta C_2(t)$ dominates $\Delta d(\beta, t)$ [31], which is characterized by $\Delta d(\beta, t)$ does not vary much with β. When β is outside this range, $\Delta C_1(t)$ and $\Delta C_2(t)$ jointly dominate $\Delta d(\beta, t)$, and the value of $\Delta d(\beta, t)$ varies with β.

Intuitively, we can determine this range by comparing the differences of $\Delta d(\beta, t)$ with different β. The difference function should be carefully selected, and it should show significant differences with different β. In this paper, we use the beat-to-beat duration correlation [30] to calculate the distance, which is defined as the Pearson's correlation coefficient (denoted as P) of the beat-to-beat duration sequence of $\Delta d(\beta, t)$ and the original green PPG data.

As shown in Fig. 8, the P versus β curve first decreases with the increasing β since the proportion of $\Delta C_1(t)$ in $\Delta d(\beta, t)$ is reduced. When $\Delta C_1(t)$ and $\Delta C_2(t)$ equally dominate $\Delta d(\beta, t)$, P reaches the lowest. As the proportion of $\Delta C_2(t)$ in $\Delta d(\beta, t)$ gradually increases, P rises until it remains stable. Within this stable range, $\Delta C_2(t)$ is considered to dominate $\Delta d(\beta, t)$. When β continuous to increase, the proportion of $\Delta C_1(t)$ in $\Delta d(\beta, t)$ recovers, and P increases. All the values in the stable range are candidates for β of Equ. 5. In our case, we determine it by finding the midpoint of the range. A detailed discussion about the impact of arterial pulse extraction on the system is presented in Section 8.5.

6 CONTINUOUS ABP MONITORING

In this subsection, we will discuss how to achieve accurate and user-independent ABP monitoring with the obtained arterial pulse. The core steps contain the basic model of ABP monitoring, user-independent ABP monitoring, and boosting the ABP monitoring.

Table 1: Supplement Features.

Feature	Description
$t_{a,b}$	The time interval between a and b
$t_{b,a_{+1}}$	The time interval between b and a_{+1}
HR	Heat rate
$A_{e,a_{+1}}/A_{a,e}$	Area ratio of e to a_{+1} and a to e under the PPG pulse
$H_{a,b}$	The amplitude difference between a and b
$H_{a,e}$	The amplitude difference between a and e

a, b, e, and a_{+1} are fiducial points of APG waveform.
α of Equ. 5 is set to 1.

6.1 Basic Model

RWTT estimation: to extract RWTT from the processed PPG data, we first segment the APG as the cardiac cycles based on the fact that onset points manifest in the form of maximum points of PPG. Intuitively, we can apply the sliding window method combined with a threshold to detect onset points. However, PPG waveform amplitude varies from time to time and across people. Finding a threshold suitable for everyone is extremely difficult. Hence, we use the Automatic Multiscale-based Peak Detection (AMPD) [45], which has been reported useful for peak detection of periodic and quasi-periodic signals. AMPD determines the window size by searching from a window that results in the maximum number of local maxima from 0.5 s to 2 s. Such a method avoids selecting a fixed threshold for cardiac cycle segmentation.

After segment beat-to-beat sequence from PPG data, we calculate beat-to-beat APG data to detect fiducial points. Specifically, we detect b by finding the point at which APG has the largest amplitude. Then, e is determined as the minimum point after b. Similarly, a is identified by locating the minimum point before b. Finally, c and d are located by detecting extremes of APG signal between b and e.

ABP estimation: as discussed in Section 2.3, RWTT is measured as the time interval between a and e in APG waveform. As RWTT is inversely related to pulse wave velocity (PWV), it has a strong correlation with ABP. Thus, we can initially calculate the ABP as below equation [35]:

$$ABP = \gamma \cdot PWV + \eta, \tag{7}$$

where constants γ and η are user-specific parameters .

6.2 User-Independent ABP Monitoring

The above basic ABP estimation model depends on the individual characteristics. Thus, the corresponding parameters generally need to be learned through calibration procedures. However, collecting sufficient data from each user for calibration is troublesome, which limits the development and application of such methodology. In addition, these mechanism ignores season effects, time of day, and other factors, therefore the accuracy is less than international standards. Thus, researchers have enforced elaborated calibration procedures, which mainly extract vascular correlation features and use machine learning algorithms.

Inspired by these works, we carefully survey plenty of features for ABP monitoring and design a Bidirectional Long Short Term Memory (BLSTM)-based Hybrid Neural Network (HNN) to enable

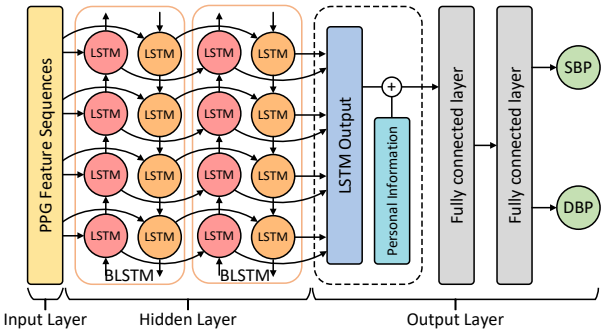

Figure 9: Structure of the designed HNN model.

user-independent ABP monitoring. Specifically, we compare the multicollinearity between candidate features and their Pearson correlation coefficient with the reference ABP. We select 6 kinds of extractable features, which are summarized in Table 1. These features are the most significant ABP features and avoid collinearity that leads to unreliable machine learning models.

Thus, these selected features are input into the BLSTM-based HNN to enable user-independent ABP monitoring. BLSTM is a popular scheme for modeling time sequence data, and it has been successfully applied to physiological signal estimation [1, 29]. However, simple stacked BLSTMs only obtain a limited accuracy in estimation takes. Thus, we design the HNN, which incorporates BLSTM and several advanced techniques. HNN combines the advantages of each layer of the network model, which allows for achieving high estimation accuracy. Fig. 9 shows the designed network structure, which consists of three parts, the input layer, the hidden layer, and the output layer. The input layer takes beat-to-beat RWTT and six vascular characteristic features as input. Before being fed to the network, features are normalized by min-max-scaling. In the hidden layer, forward LSTM and backward LSTM work together to derive the hidden information of the input feature sequences and build up a progressively higher-level representation of features. We develop two BLSTMs in the hidden layer since using two layers provides the optimum balance between complexity and accuracy. Section 7.4.2 shows details of network structure.

Since ABP changes with many physiological factors, we add a layer after the BLSTM to calibrate ABP. At the i-th timestep, the output of this layer is calculated as

$$O_s^i = W_P \cdot PI + O_{BLSTM}^i, \tag{8}$$

where W_P is the weights, O_{BLSTM}^i is the output of BLSTMs. PI is the personal information, which we define as PI=[gender, age]$^{\mathrm{T}}$ because these data are available in the training dataset. However, biometrics such as weight, height, BMI, cardiac output, etc., can be integrated into the personal information vector PI if available.

Besides, there are two fully connected layers in the output layer. They are used to learn the calibration function. Given the input O_s^i, the output y=[DBP, SBP]$^{\mathrm{T}}$ is defined by

$$y = W_{FC} \cdot O_s^i + b_{FC}, \tag{9}$$

where W_{FC} is the weight and b_{FC} is the bias. The network is trained to minimize the difference between predicted ABP and reference ABP.

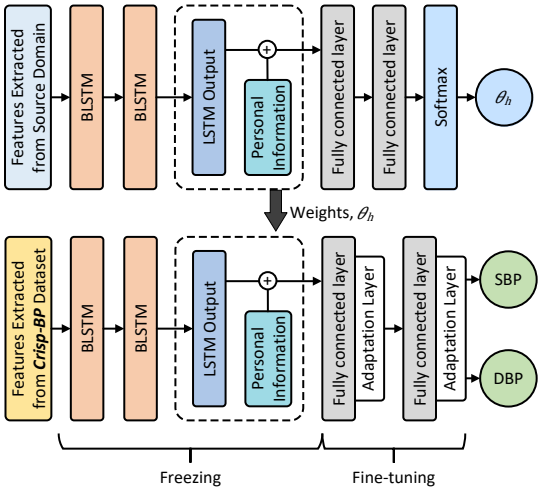

Figure 10: Improved HNN model structure and transfer learning process.

6.3 Boosting the ABP Monitoring

The above *User-Independent ABP monitoring* model requires collecting data from different gender and age to accommodate variations of ABP for different individual. However, it is hard and takes a lot of effort to collect sufficient data. To relieve the pain of data collection, we propose to use the transfer learning technique. The idea is to find a related source domain to learn general knowledge and use it to improve the learning of a model on our target domain. Data from the source domain can compensate for the scarcity of data on the target domain. Specifically, we obtain the source domain from an online dataset MIMIC III [27].

The MIMIC III database contains physiologic signals and time series of vital signs captured from ICU patients. It contains 67, 830 record sets from 30, 000 patients aged 16 or above. The median age of these patients is 65.8 years, 55.8% of patients are male, and 44.1% are female. We use the subset of patients with high-quality fingertip PPG and ABP for training the hybrid neural network. Each record has different lengths, most are a few days in duration, but some are shorter, and others are several weeks long.

Fig. 10 shows the transfer learning strategy and the improved structure of the BLSTM-base model. We add an adaptation layer after each fully connected layer to perform domain shift. During training, we use data from the source domain to train a well-performed model that minimizes the difference between associated ABP values and the predicted results. Then, we initialize a new network with weights and bias of model learned on source domain. After that, we freeze the hidden layer and personal information calibration layer. By fine-tuning weights of the fully connected layers in the output layer, we obtain the final model on *Crisp-BP*'s domain.

Domain loss (DL) is the key parameter in the adaptation layer, which is defined as

$$DL = \sum MAE_h \cdot \theta_h, \tag{10}$$

where θ_h is the weight of the h-th adaptation layer in domain loss function, which is the output by a softmax layer. MAE_h represents

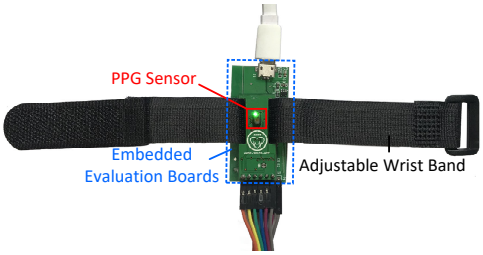

Figure 11: *Crisp-BP* prototype.

the mean absolute value of the error between the MIMIC III feature series and the *Crisp-BP* feature set.

The loss of *Crisp-BP* consists of two parts: DL, and the sum of the Mean Square Error (MSE) of diastolic blood pressure (DBP) and systolic blood pressure (SBP), expressed as

$$Loss = DL + \frac{1}{n}\sum_{i=1}^{n}[(SBP_{p_i} - SBP_{l_i})^2 + (DBP_{p_i} - DBP_{l_i})^2], \quad (11)$$

where n is the length of input sequence. SBP_{p_i} and DBP_{p_i} denote the predicted ABP results, SBP_{l_i} and DBP_{l_i} are true value of ABP records. Overall, *Crisp-BP* achieves the mean estimation error of 0.86 mmHg and 1.67 mmHg for diastolic blood pressure (DBP) and systolic blood pressure (SBP), respectively. Experiment details are presented in Section 7.3.

7 EVALUATION

In this section, we present the implementation, experiment set-up, and evaluation results of *Crisp-BP*.

7.1 Implementation

7.1.1 Sensing Prototype. We notice that existing manufacturers only provide heart rate readings but do not provide direct access to raw PPG data. We implement *Crisp-BP* with a proof-of-concept prototype as shown in Fig. 11. The prototype consists of a commodity PPG sensor, an adjustable wrist band, and an embedded evaluation board for PPG sensor. The PPG sensor and embedded evaluation board are tied together as an alternative to smartwatches.

7.1.2 Machine Learning Pipeline. We develop the neural network model use TensorFlow, Keras, and Sklearn. For the neural network models, we use a hidden layer with 2 BLSTM layers, 14 neurons per layer, embedding dropout 0.2, and batch size 32. In the training phase, we use adaptive moment estimation (Adam) optimizer with a standard setting.

7.2 Setup and Methodology

7.2.1 Data Collection. There is no state-of-art dataset that simultaneously monitors ABP and two-wavelength wrist PPG. Therefore, we collect the dataset to implement and evaluate *Crisp-BP*. All data are collected following an experimental protocol approved by the ethical review board of the institute. During four months, 35 participants (17 male and 18 female aging between 19 to 50) are recruited in this study. All participants are selected from students and faculty of the institute. They have no known medical conditions related to our evaluation. Experiments are conducted in a quiet laboratory at a comfortable temperature. The ground truth of ABP is provided by an FDA-approved, arm-cuff ABP measurement device Omron U30 [7]. Following the standard validation procedure [48], all participants sit with back supported, legs uncrossed, and arm-cuff is held at heart level to obtain accurate ground truth. ABP measurements are alternated between the cuff device and the *Crisp-BP* implemented wearable band, and measurements are performed with 60 seconds intervals. The process takes about ten minutes. To accommodate slight sensor position differences, we encourage participants to wear the band 1-3 finger-widths above their wrist bone. Specifically, we collect at least ten sessions from each participant in four months. Between each session, the participants are asked to take a 10 minutes break.

Table 2: Evaluation Measurements.

Measurement	Formula
Mean Error	$ME = \frac{\sum_{i=1}^{n}(p_i - r_i)}{n}$
Standard Deviation	$STD = \sqrt{\frac{\sum_{i=1}^{n}(p_i - r_i - ME)^2}{n}}$
Sample Pearson's Correlation Coefficient	$P = \frac{\sum_{i=1}^{n}(r_i - \bar{r})(p_i - \bar{p})}{\sqrt{\sum_{i=1}^{n}(r_i - \bar{r})^2}\sqrt{\sum_{i=1}^{n}(p_i - \bar{p})^2}}$

To validate *Crisp-BP*'s effectiveness for continuous monitoring, we conduct a 24-hour experiment that compares the ambulatory ABP ground truth with the estimated results. Besides, we conduct experiments with different PPG sensors and sampling frequencies to evaluate *Crisp-BP* against various issues. Furthermore, to understand the performance of key algorithms, we ask participants to collect data with various contact pressures and network structures. Overall, we collect more than 51,750 minutes of PPG recordings for evaluation.

7.2.2 Evaluation Methodology. Three measurements, including mean error (*ME*), standard deviation of mean error (*STD*), and sample Pearson's correlation coefficient (*P*) are used in this paper to measure the accuracy of the proposed method. Formulas for these measurements are shown in Table 2, where r_i is the reference value of ABP from ground truth recordings, p_i is the predicted value of *Crisp-BP*, $\bar{r}$ and $\bar{p}$ are mean of reference ABP and predicted ABP, respectively, and n is the number of samples.

7.3 Overall Performance

To understand the performance of the designed system for user-independent ABP monitoring, we evaluate *Crisp-BP* by conducting leave-one-participant-out validation, where we use data from one participant for testing and data from the remaining participants for training. Fig. 12 shows the Bland-Altman plots for the estimated SBP and DBP. The results are from all combinations of training and testing data. The x-axis is the average reference ABP of all participants, and the y-axis is the estimation error. The mean errors of DBP and SBP are 0.86 mmHg and 1.67 mmHg, the standard deviation of mean error of DBP and SBP are 6.55 mmHg and 7.31 mmHg, respectively. The result confirms that *Crisp-BP* is accurate for user-independent ABP monitoring. Besides, the red line indicates the mean error, and the black lines indicate the limits of agreement (ME $\pm 1.96 \times STD$). More than 95% of the points lie within the limit of agreement in SBP and DBP, which ensures great accuracy in practical usage.

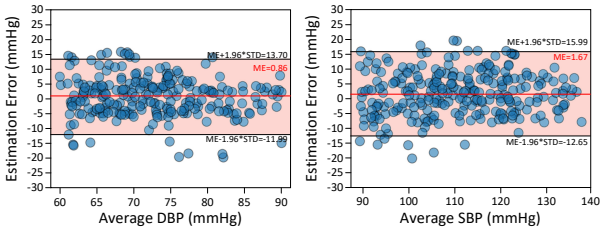

(a) DBP (b) SBP

Figure 12: Bland–Altman diagram of DBP and SBP.

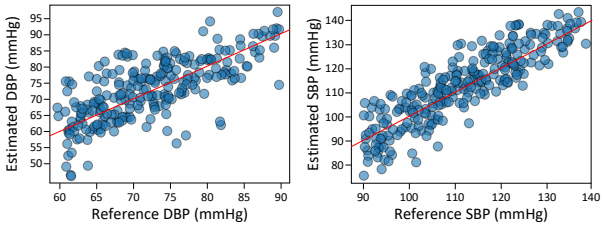

(a) DBP (b) SBP

Figure 13: Correlation diagram of DBP and SBP.

Fig. 13 shows the correlation diagram of the estimated results and the reference value. The x-axis represents the reference BP value from ground truth records, and the y-axis represents the estimated results. Points on the red line have identical values, and the distance to the red line is proportional to the error. We can observe that points are clustered around the red line, which suggests a close correlation. Specifically, the Pearson's correlation coefficients for SBP and DBP are 0.88 and 0.82, respectively.

Table 3 compares our results with the requirement for the Association for the Advancement of Medical Instruments (AAMI) standard [48], *Crisp-BP* satisfies the recommended error boundary as defined by the AAMI. Table 4 compares our results with the requirement for the Britain Hypertension Society (BHS) standard [39]. We have achieved grade A for DBP and SBP. The results demonstrate high estimation accuracies for SBP and DBP.

7.3.1 24-Hour Performance. Because accurate ground truth of ABP should be measured under controlled circumstances (e.g., sit with back supported and feet on the floor, arm supported at heart level), it is not feasible to conduct a beat-to-beat evaluation throughout 24 hours. Therefore, to collect the continuous PPG data and corresponding ground truth, we ask each volunteer to alternately wear our prototype and an arm-cuff ABP measurement device (Omron U30) every 30 minutes during the day and every hour at night. Fig. 14 shows the 24-hour estimation error for DBP and SBP. We can observe that *Crisp-BP* performs better during the day, and the estimation error of DBP and SBP fluctuates below 3.2 mmHg, which confirms the effectiveness of *Crisp-BP*. Moreover, DBP estimates from 3 o'clock to 5 o'clock receive relatively high errors. We carefully check the results of different participants and find that four participants contribute the most to the error during 3-5 AM. They report that being interrupted during sleeping and no enough sleep affect their emotion and heart rate. The study of those cases is left as future work.

Table 3: Comparison of *Crisp-BP* with AAMI standard.

		ME (mmHg)	STD (mmHg)
Crisp-BP	DBP	0.86	6.55
	SBP	1.67	7.31
AAMI	SBP and DBP	⩽5	⩽8

Table 4: Comparison of *Crisp-BP* with BHS standard.

		Cumulative Error Percentage		
		⩽5 mmHg	⩽10 mmHg	⩽15 mmHg
Crisp-BP	DBP	76.73%	91.43%	97.96%
	SBP	65.66%	87.17%	96.23%
BHS	Grade A	60%	85%	95%
	Grade B	50%	75%	90%
	Grade C	40%	65%	85%

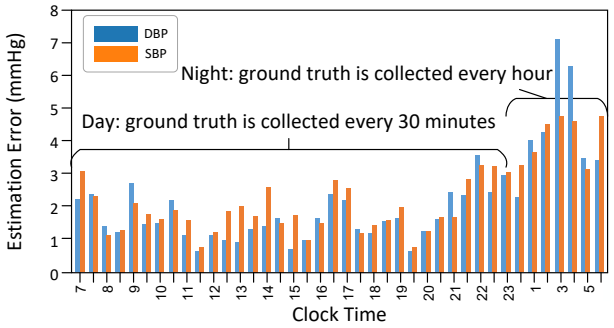

Figure 14: 24-hour performance.

7.4 Key Algorithm Performance

7.4.1 Effectiveness of Contact Pressure Estimation. As declaration in Section. 4.1, the PPG waveform is highly sensitive to the contact pressure between the sensor and human skin, which will impact the accuracy of ABP estimation. Therefore, *Crisp-BP* proposes a contact pressure estimation method to assist users in adjusting the wearable tight or loose and maintain a proper contact pressure during data collection. In this subsection, we will first study the impact of different contact pressure and then evaluate the performance of the proposed contact pressure estimation method.

We first evaluate the ABP estimation performance under three types of contact pressure (i.e., lower than optimal contact pressure (OCP), equal to OCP, and higher than OCP). The OCP is the pressure associates with the highest amplitude of the AC component. The ABP estimation error between each type of contract pressure and ground truth is shown in Fig. 15. We can find that the case of equal to OCP achieves the lowest error for both DBP and SBP. The case of lower than OCP has higher errors than other cases. The reason may rely on the relative motions between the PPG sensor and skin, which introduce more noise in the PPG data. This result further demonstrates the necessity of contact pressure control.

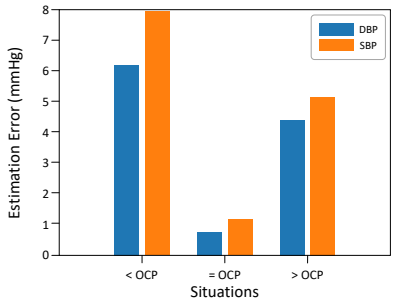

Figure 15: Impact of contact pressure.

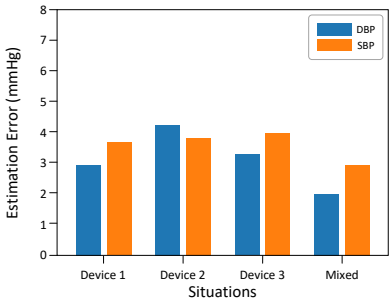

Figure 16: Impact of PPG sensor.

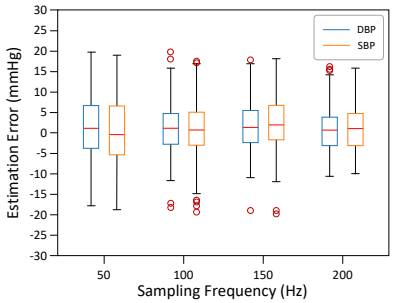

Figure 17: Impact of sampling frequency.

Table 5: System performance without transfer learning vs. with transfer learning.

		ME (mmHg)	STD (mmHg)
Without Transfer Learning	DBP	4.88	12.24
	SBP	7.30	18.59
With Transfer Learning	DBP	0.86	6.55
	SBP	1.67	7.31

Then, to validate the effectiveness of our contact pressure estimation method, we attach a 7.6 mm round head thin film pressure sensor alongside the PPG sensor to obtain the ground truth of contact pressure. Overall, the proposed method receives a mean error of 6.12 g, a standard deviation of 11.63 g, and a Pearson's correlation coefficient of 0.65. When contact pressure is divided into three classes of lower than OCP, equal to OCP, and higher than OCP, 96.81% samples are correctly classified. As the results implied, our system can effectively estimate contact pressure and provide a basis for *Crisp-BP*.

7.4.2 Impact of ABP Monitoring Model Structure. The proposed hybrid neural network model is based on BLSTM. The number of BLSTM layers, the memory cell at each layer, and batch size significantly impact the ABP estimation accuracy. Exploiting more BLSTM layers and more memory cells can better derive the hidden relationship between ABP and RWTT and other features but lead to higher computational costs. Besides, convergence may not be found when using too many BLSTM layers. We compare different combinations of model parameters, including neural cells, batch size, and the number of BLSTM layers. We find that 2 layer, 14 neurons per layer, embedding dropout 0.2, and batch size 32 provide the optimum balance between complexity and accuracy. Therefore, we chose the above parameters as our default network through empirical studies. Detailed results are ignored due to the space limit.

7.4.3 Effectiveness of Transfer Learning Method. The goal of developing the transfer learning method is to boost user-independent ABP monitoring when only limited training data is obtained. We compare our method with transfer learning to the same method without transfer learning. Table 5 shows the comparison. Clearly, the proposed transfer learning can significantly reduce the estimation error for both DBP and SBP. This validates the effectiveness of transfer learning.

7.5 System Robustness

7.5.1 Impact of Sensor Diversity. Implementation on different devices is a critical aspect of ABP monitoring algorithms. Therefore, we conduct experiments with data collected by three commodity PPG sensors, including the MAX30105 (denoted as device 1), MAX30101 (denoted as device 2), and AS7026GG (denoted as device 3), which differ in size and optical hardware. We use data collected from one device for testing and data from the remaining devices for training. Besides, we conduct five-fold cross-validation by training a network model with 75% mixed data from all devices and testing the model with the reminding 25% data (denoted as mixed). Fig. 16 shows the mean error of APB estimation under different types of PPG sensors. We can observe that sensor diversity only has a slight impact on the system performance. After careful analysis, we find that the sensor diversity mainly affects the amplitude and area-related vascular characteristic features, while time interval-related features and time-resolved RWTT have high quality. The proposed network effectively harnesses the variation of features, leading to a mean error of less than 5 mmHg. This result indicates that *Crisp-BP* works well across devices.

7.5.2 Impact of Sampling Frequency. On the one hand, a higher sampling frequency enables more samples to be collected, which benefits the analysis of artery volume change. However, it certainly will lead to higher computational costs. On the other hand, insufficient sampling leads to errors in RWTT estimation and further reduces the ABP monitoring accuracy. As off-the-shelf wearables only support a limited sampling frequency, we study the impact of sampling frequency by varying the frequency from 50 Hz to 200 Hz. Fig. 17 shows the box-and-whisker plot of SBP and DBP with different sampling frequencies. The lowest point is the minimum of the estimation error, and the highest point is the maximum of the estimation error. The box is drawn from Q1 (the median of the *lower* half of the dataset) to Q3 (the median of the *upper* half of the dataset) with a horizontal red line drawn in the middle to denote the median. We can observe that error decrease with the increase of sampling frequency, and DBP receives better estimation performance than SBP. Off-the-shelf smartwatch and fitness can flash their LED lights hundreds of times per second [6], which can obtain acceptable results based on the experiment. Therefore, *Crisp-BP* is compatible with the device that supports various sampling frequencies.

Table 6: Comparisons of *Crisp-BP* with typical works on portable ABP measuring via PPG signal.

Comparison items	Glabella [25]	SeismoWatch [17]	Seismo [55]	Naptics [16]	eBP [14]	*Crisp-BP*
Method	PTT	PTT	PTT	PTT	CPA	RWTT
Subject	4	13	9	6	35	35
Device type	Glasses	Wristband	Phone	Shorts	In-Ear	Wristband
Auxiliary tools	None	Accel	Accel	Accel+elec+oxi	Balloon	None
Passive sensing	Yes	No	No	Yes	No	Yes
Scenario	Daytime	Instant	Instant	Night	Instant	Daytime+Night
Comfort level	High	Middle	Middle	Middle	Middle	High
SBP ME/STD (mmHg)	±10	4.8	N/A	N/A	1.8/7.2	1.67/7.31
DBP ME/STD (mmHg)	N/A	2.9	1.3/6.9	N/A	-3.1/7.9	0.86/6.55

* PTT, CPA stand for pulse transit times, change of pulse amplitude, respectively. Accel, elec, and oxi represent accelerometer, electrodes, and oximeter, respectively.

7.6 Comparison with Typical Related Works

Table 6 shows the comparison results between *Crisp-BP* and other typical works on portable ABP measuring via PPG signal in terms of the used method, subject number, the type of portable device, auxiliary sensors/tools, passive or participatory sensing, working scenario, comfort level, and the reported accuracy of APB estimation (i.e., the mean error/standard deviation of SBP and DBP).

These typical works exploit the Change of Pulse Amplitude (CPA) [14] or Pulse Transit Times (PTT) [16, 17, 25, 55] to estimate the ABP. To change the artery volume, the former work requires a balloon to press the artery. This procedure needs to be triggered manually by the user. Therefore, this method only works in an instant manner. Besides, the ear will be stuffed by the inflation balloon, which reduces the user's comfort certainly. In contrast, *Crisp-BP* can work on a wristband device in a passive manner, which has less impact on the user comfort.

Meanwhile, the later works based on PTT can be embedded on the glasses, wristband, phone, and shorts, respectively. To calculate the PPT, SeismoWatch [17], Seismo [55], and Naptics [16] also need the cooperation from additional sensors (e.g., accelerometer, oximeter). Among these works, Glabella [25] and Naptics [16] support long-term working scenarios (i.e., during the daytime and night, respectively). Comparing with them, *Crisp-BP* can work during both daytime and night without any additional sensors or tools.

8 DISCUSSION

8.1 Impact of Lighting Condition

PPG is an optical technique that detects blood flow by illuminating the skin and measuring light absorption. The PPG sensor may pick up ambient light, which significantly affects the PPG waveform. This can be addressed by capturing the light level when LEDs are off and subtracting it from the collected data.

8.2 Impact of Skin Tone

Variations in human skin tone affect the absorption of light, and different skin tones have different impacts on the green-light-PPG and infrared-light-PPG. For example, darker skin absorbs more green light than light skin. This impairs the extraction of arterial pulse and might limit the scope of application. Yellow light with a longer wavelength than green light can reach deeper tissue of the skin. The combination of yellow and infrared light not only retains depth-resolved information but also reduces the impact of skin color. Future manufacturers can use yellow light instead of green light to reduce the impact of skin tones.

8.3 Impact of Wrist Position

Crisp-BP obtains the APB value mainly rely on the accurate RWTT estimation. However, the relative position between the wrist and the heart will influence the RWTT estimation since the velocity of blood flow will change. For example, when users raise their wrists above their heart level, the velocity of blood flow on the wrist will be reduced. To achieve an accurate ABP estimation, we suggest users to place his/her wrist close to the heart level when sitting or standing. Besides, when the user is lying flat (e.g., take a rest or sleeping), he/she should lay his/her wrist flat too.

8.4 Impact of Body Movement

Wrist-worn devices are usually associated with body movements from activities of daily living. The impact of body movement can deform the PPG signal, which leads to errors in the ABP estimation results. Luckily, a lot of research efforts have been made to suppress and reduce the noise caused by body movement, such as analyze the difference between green PPG and infrared PPG, and apply the semi-blind source separation method [15]. Such a method can effectively cancel the impact of body movement in PPG signal.

8.5 Impact of Arterial Pulse Extraction

The proposed arterial pulse extraction method aims to remove the capillary pulse and obtain the artery pulse. Then, we measure the RWTT from the extracted arterial pulse. The algorithm parameter β only needs to meet the conditions mentioned in Sec. 5.2 because different values of β mainly affect the waveform amplitude. While RWTT is a time-interval descriptor, *Crisp-BP* can measure accurate RWTT despite there is a small error in waveform amplitude.

9 RELATED WORK

To detect or monitor medical problems, many efforts have been made to obtain vital signs [20]. Arterial blood pressure (ABP) is one of the main vital signs for routine monitoring. Previous studies on ABP monitoring vary in sensing modalities and sensor placement. The most commonly used clinical ABP monitoring method

is to block arterial blood flow with a cuff and determine the ABP based on Korotkoff sounds [54] or oscillometric method [44] in the discharge process. However, environmental noise can interfere with the Korotokff sounds, which makes the results inaccurate. In contrast, volume clamp [42], tonometry [43], and ultrasonic [13] are proposed to monitor the blood waveform. Although they provide continuous and non-invasive monitoring results, using special equipment makes them difficult to be adopted widely. Moreover, these methods involve a vessel compression process. Study [23] has revealed risks of tissue hypoxia on the distal side that applied pressure.

As wearable devices are increasingly pervasive and common in our daily lives, advancements in research have been leading to increased innovation in health care applications. HeartGuide [8] and eBP [14] enable oscillometric measurements of ABP in wristwatch and in-ear wearable, respectively. Using oscillometric measurement is accurate, but these methods are still limited to measuring ABP a few times per day as repeated cuff inflation is uncomfortable.

To reduce discomfort, research efforts have been made to develop cuffless technologies [24, 34] for ABP monitoring. The most commonly used are based on the time delay of a blood pulse at two different sites, i.e., pulse transit time (PTT) [38, 40] and pulse arrival time (PAT) [19, 28]. These parameters can be obtained by measuring the time interval between ECG and PPG, or between two PPG signals, collected simultaneously from two positions. For example, VivoWatch [2] and Apple Watch [6] incorporate ECG and PPG sensors into the smartwatch. ABP can be tracked by measuring PTT and PAT from the time interval between ECG and PPG. However, they require users to press fingers on the ECG pad throughout data collection. SeismoWatch [17] and Seismo [55] measure the vibration of the heart valve and the pulse at the limbs using a watch and a smartphone, respectively. They require the user to press the measuring device on the sternum. Sugita *et al.* [49] estimate ABP using video captured at different heights from the heart, but they require users to sit in a fixed position in front of the camera. A common limitation of these methods is the need for user effort, which is inconvenient and degrades user experience.

To minimize such impact, approaches that require no user effort have been proposed. Glabella [25] adopts PPG sensors and constructs a pair of glasses to measure PTT from different sites on the user's face. However, Glabella is limited to daytime systolic ABP monitoring. For night-time monitoring, Naptics [16] incorporates a series of physiological sensors and develops a PTT-based system woven into compression shorts. Vahdani-Manaf [53] uses a ring-shaped PPG sensor for collecting PPG with infrared, red, green, and blue LEDs. Liu *et al.* [30, 32] develop a multi-wavelength PPG sensor to record PPG signals with infrared, yellow, green, and blue LEDs. They mainly extract time differences (TD) between separate pairs of PPG signal with different wavelengths and apply the modified PTT-based method to monitor ABP. The calculated TD is about a few tens of milliseconds, which is energy-consuming to obtain accurate values. In addition to limited usage scopes, they rely on prototypes unavailable to consumers. Moreover, these methods are affected by season effects, time of day, and other factors. Therefore, the accuracy is less than international standards.

Extracting features from PPG, ECG [21, 47, 58] and using machine learning methods usually achieve enhanced accuracy and more consistent output. Nevertheless, these approaches have deficiencies in model training. The training dataset must be sufficiently big and cover different gender and age to accommodate variations of ABP for each individual, which is inconvenient and usually takes much effort.

From another perspective, reflected wave transit time (RWTT) provides a new opportunity for ABP monitoring. RWTT is defined as the transit time between the forward blood flow and the backward blood flow at the same position, which can be measured from blood flow acceleration [51, 57]. However, measuring blood flow acceleration requires mounting special accelerometers around the artery, which is invasive. Besides, Wang *et al.* [56] and Mitchell *et al.* [37] respectively investigate using non-invasive pulse wave tonometer to measure RWTT for arterial stiffness assessment. However, continuous measurement is not accurate due to variations in force and angle when manually holding the sensing device against the measurement site as well as other issues [9].

Compared with existing efforts, our design only employs a single commodity PPG sensor available in wrist-worn devices. While using our system, the users naturally wear a smartwatch or fitness tracker, which fosters continuousness, comfort, and convenience. By profiling the blood volume change and constructing an effective hybrid neural network model, our design can measure accurate RWTT and generate accurate ABP values. More importantly, *Crisp-BP* is user-independent, which can be generalized to new users without acquiring their training data. Therefore, *Crisp-BP* is promising for practical usage.

10 CONCLUSION

This paper presents *Crisp-BP*, which is the first ABP monitoring system that fosters continuousness, comfort, convenience, accuracy, and user-independence. *Crisp-BP* utilizes a single PPG sensor available in wrist-worn devices (e.g., smartwatches and fitness trackers). It works by profiling volume change with the captured light reflection intensity and measuring RWTT to produce accurate ABP. Specifically, we propose a set of algorithms to remove capillary interference in arterial pulse and compact contact pressure-sensitive deficiency. After extracting RWTT and supplement features from PPG data, a BLSTM-based hybrid neural network is developed. To address data scarcity, we propose a transfer learning method that extracts general knowledge from a large amount of online PPG data. Then we transfer it to a new model in *Crisp-BP*'s domain. Extensive experiments involving 35 participants demonstrate that *Crisp-BP* successfully takes one step forward to provide accurate ABP monitoring with the estimation error of 0.86 ± 6.55 mmHg and 1.67 ± 7.31 mmHg for DBP and SBP, respectively. These errors are within the acceptable range regulated by the AAMI protocol. We believe that *Crisp-BP* has the great potential to improve the diagnosis and control of hypertension and increase the utility of wrist-worn devices.

11 ACKNOWLEDGMENTS

We thank our anonymous shepherd and reviewers for their invaluable feedback and comments. This work is supported in part by National Natural Science Foundation of China 62072040, 61772077 and Beijing Municipal Natural Science Foundation 4192051.

REFERENCES

[1] 2020. Sleep staging by bidirectional long short-term memory convolution neural network. *Future Generation Computer Systems* 109 (2020), 188–196.

[2] 2021. Asus VivoWatch BP. https://www.asus.com/us/VivoWatch/ASUS-VivoWatch-BP-HC-A04/

[3] 2021. Honor band support infrared technology to avoid the green light from disturbing your sleep. https://www.hihonor.com/global/products/wearables/honorband5/

[4] 2021. HUAWEI Watch has four sensors for measureing heart rate. https://consumer.huawei.com/ph/wearables/watch-gt-2e/specs/

[5] 2021. Mi Band 5 NFC version also supports infrared monitoring, which can avoid the interference of visible green light at night. https://xiaomi-mi.com/mi-band/mi-band-5-nfc-edition/

[6] 2021. Monitor your heart rate with Apple Watch. https://support.apple.com/en-ae/HT204666.

[7] 2021. OMRON Digital Blood Pressure Monitor. http://www.omronhealthcare.com.cn/home-product/blood-pressure-meter/U30.

[8] 2021. OMRON HeartGuide. https://omronhealthcare.com/products/heartguide-wearable-blood-pressure-monitor-bp8000m/

[9] 2021. The SPT-301 non-invasive pulse tonometer cannot be used to continuously measure absolute arterial pressure in any accurate or meaningful way. https://www.adinstruments.com/support/knowledge-base/can-millar-spt-301-non-invasive-pulse-tonometer-be-calibrated-read-arterial.

[10] John Allen. 2007. Photoplethysmography and its application in clinical physiological measurement. *Physiological measurement* 28, 3 (2007), R1.

[11] H Harry Asada, Phillip Shaltis, Andrew Reisner, Sokwoo Rhee, and Reginald C Hutchinson. 2003. Mobile monitoring with wearable photoplethysmographic biosensors. *IEEE Engineering in Medicine and Biology Magazine* 22, 3 (2003), 28–40.

[12] Wesley B Baker, Ashwin B Parthasarathy, David R Busch, Rickson C Mesquita, Joel H Greenberg, and AG Yodh. 2014. Modified Beer-Lambert law for blood flow. *Biomedical optics express* 5, 11 (2014), 4053–4075.

[13] Iain FS Black, Niran Kotrapu, and Harold Massie. 1972. Application of Doppler ultrasound to blood pressure measurement in small infants. *The Journal of pediatrics* 81, 5 (1972), 932–935.

[14] Nam Bui, Nhat Pham, Jessica Jacqueline Barnitz, Zhanan Zou, Phuc Nguyen, Hoang Truong, Taeho Kim, Nicholas Farrow, Anh Nguyen, Jianliang Xiao, et al. 2019. eBP: A wearable system for frequent and comfortable blood pressure monitoring from user's ear. In *The 25th Annual International Conference on Mobile Computing and Networking*. 1–17.

[15] Yetong Cao, Qian Zhang, Fan Li, Song Yang, and Yu Wang. 2020. PPGPass: Nonintrusive and Secure Mobile Two-Factor Authentication via Wearables. In *IEEE INFOCOM 2020 - IEEE Conference on Computer Communications*. 1917–1926.

[16] Andrew Carek and Christian Holz. 2018. Naptics: Convenient and continuous blood pressure monitoring during sleep. *Proceedings of the ACM on Interactive, Mobile, Wearable and Ubiquitous Technologies* 2, 3 (2018), 1–22.

[17] Andrew M Carek, Jordan Conant, Anirudh Joshi, Hyolim Kang, and Omer T Inan. 2017. SeismoWatch: wearable cuffless blood pressure monitoring using pulse transit time. *Proceedings of the ACM on interactive, mobile, wearable and ubiquitous technologies* 1, 3 (2017), 1–16.

[18] Anand Chandrasekhar, Mohammad Yavarimanesh, Keerthana Natarajan, Jin-Oh Hahn, and Ramakrishna Mukkamala. 2020. PPG sensor contact pressure should be taken into account for cuff-less blood pressure measurement. *IEEE Transactions on Biomedical Engineering* 67, 11 (2020), 3134–3140.

[19] Wenxi Chen, Toshiyo Kobayashi, Seiichi Ichikawa, Yasuo Takeuchi, and Tatsuo Togawa. 2000. Continuous estimation of systolic blood pressure using the pulse arrival time and intermittent calibration. *Medical and Biological Engineering and Computing* 38, 5 (2000), 569–574.

[20] Zhe Chen, Tianyue Zheng, Chao Cai, and Jun Luo. 2022. MoVi-Fi: Motion-robust Vital Signs Waveform Recovery via Deep Interpreted RF Sensing. In *The 27th Annual International Conference on Mobile Computing and Networking*. 1–14.

[21] Kefeng Duan, Zhiliang Qian, Mohamed Atef, and Guoxing Wang. 2016. A feature exploration methodology for learning based cuffless blood pressure measurement using photoplethysmography. In *2016 38th Annual international conference of the IEEE engineering in medicine and biology society (EMBC)*. 6385–6388.

[22] Yuancheng Fung. 2013. *Biomechanics: circulation*. Springer Science & Business Media.

[23] JS Gravenstein, David A Paulus, Jeffrey Feldman, and Gayle McLaughlin. 1985. Tissue hypoxia distal to a Penaz finger blood pressure cuff. *Journal of clinical monitoring* 1, 2 (1985), 120–125.

[24] Brian Gribbin, Andrew Steptoe, and Peter Sleight. 1976. Pulse wave velocity as a measure of blood pressure change. *Psychophysiology* 13, 1 (1976), 86–90.

[25] Christian Holz and Edward J Wang. 2017. Glabella: Continuously sensing blood pressure behavior using an unobtrusive wearable device. *Proceedings of the ACM on Interactive, Mobile, Wearable and Ubiquitous Technologies* 1, 3 (2017), 1–23.

[26] Hsin Hsiu, Chia-Liang Hsu, and TL Wu. 2011. Effects of different contacting pressure on the transfer function between finger photoplethysmographic and radial blood pressure waveforms. *Proceedings of the Institution of Mechanical Engineers, Part H: Journal of Engineering in Medicine* 225, 6 (2011), 575–583.

[27] Alistair EW Johnson, Tom J Pollard, Lu Shen, Li-Wei H Lehman, Mengling Feng, Mohammad Ghassemi, Benjamin Moody, Peter Szolovits, Leo Anthony Celi, and Roger G Mark. 2016. MIMIC-III, a freely accessible critical care database. *Scientific data* 3, 1 (2016), 1–9.

[28] Mohammad Kachuee, Mohammad Mahdi Kiani, Hoda Mohammadzade, and Mahdi Shabany. 2016. Cuffless blood pressure estimation algorithms for continuous health-care monitoring. *IEEE Transactions on Biomedical Engineering* 64, 4 (2016), 859–869.

[29] Eldrid Langesaeter, Leiv Rosseland, and Audun Stubhaug. 2008. Continuous Invasive Blood Pressure and Cardiac Output Monitoring during Cesarean Delivery A Randomized, Double-blind Comparison of Low-dose versus High-dose Spinal Anesthesia with Intravenous Phenylephrine or Placebo Infusion. *Anesthesiology* 109 (11 2008), 856–63.

[30] Jing Liu, Bryan P Yan, Yuan-Ting Zhang, Xiao-Rong Ding, Peng Su, and Ni Zhao. 2018. Multi-wavelength photoplethysmography enabling continuous blood pressure measurement with compact wearable electronics. *IEEE Transactions on Biomedical Engineering* 66, 6 (2018), 1514–1525.

[31] Jing Liu, Bryan Ping-Yen Yan, Wen-Xuan Dai, Xiao-Rong Ding, Yuan-Ting Zhang, and Ni Zhao. 2016. Multi-wavelength photoplethysmography method for skin arterial pulse extraction. *Biomedical optics express* 7, 10 (2016), 4313–4326.

[32] Jing Liu, Yuan-Ting Zhang, Xiao-Rong Ding, Wen-Xuan Dai, and Ni Zhao. 2016. A preliminary study on multi-wavelength PPG based pulse transit time detection for cuffless blood pressure measurement. In *2016 38th Annual International Conference of the IEEE Engineering in Medicine and Biology Society (EMBC)*. 615–618.

[33] Marek Malik, Farrell TG, Cripps TR, and John Camm. 1990. Heart Rate Variability in Relation to Prognosis after Myocardial Infarction: Selection of Optimal Processing Techniques. *European heart journal* 10 (01 1990), 1060–74.

[34] Devin B Mccombie, Andrew T Reisner, Haruhiko H Asada, and Phillip Shaltis. 2010. Wearable pulse wave velocity blood pressure sensor and methods of calibration thereof. US Patent 7,674,231.

[35] Emmanuel Messas, Mathieu Pernot, and Mathieu Couade. 2013. Arterial wall elasticity: state of the art and future prospects. *Diagnostic and interventional imaging* 94, 5 (2013), 561–569.

[36] Katherine T Mills, Andrei Stefanescu, and Jiang He. 2020. The global epidemiology of hypertension. *Nature Reviews Nephrology* (2020), 1–15.

[37] Gary F Mitchell, Helen Parise, Emelia J Benjamin, Martin G Larson, Michelle J Keyes, Joseph A Vita, Ramachandran S Vasan, and Daniel Levy. 2004. Changes in arterial stiffness and wave reflection with advancing age in healthy men and women: the Framingham Heart Study. *Hypertension* 43, 6 (2004), 1239–1245.

[38] Jochanan E Naschitz, Stanislas Bezobchuk, Renata Mussafia-Priselac, Scott Sundick, Daniel Dreyfuss, Igal Khorshidi, Argyro Karidis, Hagit Manor, Mihael Nagar, Elisabeth Rubin Peck, et al. 2004. Pulse transit time by R-wave-gated infrared photoplethysmography: review of the literature and personal experience. *Journal of clinical monitoring and computing* 18, 5-6 (2004), 333–342.

[39] Eoin O'Brien, James Petrie, WA Littler, Michael de Swiet, Paul L Padfield, Douglas Altman, Martin Bland, Andrew Coats, Neil Atkins, et al. 1993. The British Hypertension Society protocol for the evaluation of blood pressure measuring devices. *J hypertens* 11, Suppl 2 (1993), S43–S62.

[40] Paul A Obrist, Kathleen C Light, James A McCubbin, J Stanford Hutcheson, and J Lee Hoffer. 1979. Pulse transit time: Relationship to blood pressure and myocardial performance. *Psychophysiology* 16, 3 (1979), 292–301.

[41] Hiroshi Osanai. 1984. Plethysmographic acceleration pulse wave meter. US Patent 4,432,374.

[42] Jan Penaz. 1973. Photoelectric measurement of blood pressure, volume and flow in the finger'In: Digest of the 10th International Conference on Medical and Biological Engineering. *Dresden* 104 (1973).

[43] GL Pressman and Peter M Newgard. 1963. A transducer for the continuous external measurement of arterial blood pressure. *IEEE Transactions on Bio-medical Electronics* 10, 2 (1963), 73–81.

[44] Maynard Ramsey. 1979. Noninvasive automatic determination of mean arterial pressure. *Medical and Biological Engineering and Computing* 17, 1 (1979), 11–18.

[45] Felix Scholkmann, Jens Boss, and Martin Wolf. 2012. An efficient algorithm for automatic peak detection in noisy periodic and quasi-periodic signals. *Algorithms* 5, 4 (2012), 588–603.

[46] Hangsik Shin and Se Dong Min. 2017. Feasibility study for the non-invasive blood pressure estimation based on PPG morphology: Normotensive subject study. *Biomedical engineering online* 16, 1 (2017), 1–14.

[47] Gašper Slapničar, Nejc Mlakar, and Mitja Luštrek. 2019. Blood pressure estimation from photoplethysmogram using a spectro-temporal deep neural network. *Sensors* 19, 15 (2019), 3420.

[48] George S Stergiou, Bruce Alpert, Stephan Mieke, Roland Asmar, Neil Atkins, Siegfried Eckert, Gerhard Frick, Bruce Friedman, Thomas Graßl, Tsutomu Ichikawa, et al. 2018. A universal standard for the validation of blood pressure measuring devices: Association for the Advancement of Medical Instrumentation/European Society of Hypertension/International Organization for Standardization (AAMI/ESH/ISO) Collaboration Statement. *Hypertension* 71, 3

(2018), 368–374.

[49] Norihiro Sugita, Taihei Noro, Makoto Yoshizawa, Kei Ichiji, Shunsuke Yamaki, and Noriyasu Homma. 2019. Estimation of Absolute Blood Pressure Using Video Images Captured at Different Heights from the Heart. In *2019 41st Annual International Conference of the IEEE Engineering in Medicine and Biology Society (EMBC)*. 4458–4461.

[50] JAK Suykens, Lukas Lukas, Paul Van Dooren, Bart De Moor, Joos Vandewalle, et al. 1999. Least squares support vector machine classifiers: a large scale algorithm. In *Proceedings of the European Conference on Circuit Theory and Design*, Vol. 10. Citeseer.

[51] Michael Theodor, Dominic Ruh, Katharina Förster, Claudia Heilmann, Friedhelm Beyersdorf, Hans Zappe, and Andreas Seifert. 2013. Implantable acceleration plethysmography for blood pressure determination. In *2013 35th Annual International Conference of the IEEE Engineering in Medicine and Biology Society (EMBC)*. 4038–4041.

[52] Uwe Thissen, Bülent Üstün, Willem J Melssen, and Lutgarde MC Buydens. 2004. Multivariate calibration with least-squares support vector machines. *Analytical Chemistry* 76, 11 (2004), 3099–3105.

[53] Nader Vahdani-Manaf. 2015. Biological assessments by innovative use of multi-wavelength photoplethysmographic signals time differences. *JApSc* 15, 11 (2015), 1312–1317.

[54] GA Van Montfrans, GM Van Der Hoeven, JM Karemaker, W Wieling, and AJ Dunning. 1987. Accuracy of auscultatory blood pressure measurement with a long cuff. *Br Med J (Clin Res Ed)* 295, 6594 (1987), 354–355.

[55] Edward Jay Wang, Junyi Zhu, Mohit Jain, Tien-Jui Lee, Elliot Saba, Lama Nachman, and Shwetak N Patel. 2018. Seismo: Blood pressure monitoring using built-in smartphone accelerometer and camera. In *Proceedings of the 2018 CHI Conference on Human Factors in Computing Systems*. 1–9.

[56] Kang-Ling Wang, Hao-Min Cheng, Shih-Hsien Sung, Shao-Yuan Chuang, Cheng-Hung Li, Harold A Spurgeon, Chih-Tai Ting, Samer S Najjar, Edward G Lakatta, Frank CP Yin, et al. 2010. Wave reflection and arterial stiffness in the prediction of 15-year all-cause and cardiovascular mortalities: a community-based study. *Hypertension* 55, 3 (2010), 799–805.

[57] Jiawei Yang. 2020. Blood pressure calculation method based on pulse return wave transmission time, and blood pressure monitor. US Patent 10,537,254.

[58] Yue Zhang and Zhimeng Feng. 2017. A SVM method for continuous blood pressure estimation from a PPG signal. In *Proceedings of the 9th International Conference on Machine Learning and Computing*. 128–132.